Contents lists available at ScienceDirect

iOptics

journal homepage: www.keaipublishing.com/en/journals/ioptics

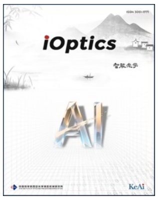

Intrinsic dark-field Fourier ptychographic diffraction tomography under non-matched illumination

Habib Ullah [a,b,c,1], Shun Zhou [a,b,c,1], Kaiyu Du [a,b,c], Zhidong Bai [a,b,c], Xingyu Huang [a,b,c], Linpeng Lu [a,b,c], Qian Chen [c,d,*], Chao Zuo [a,b,c,d,**]

[a] *Smart Computational Imaging Laboratory (SCILab), School of Electronic and Optical Engineering, Nanjing University of Science and Technology, Nanjing, Jiangsu Province 210094, China*
[b] *Smart Computational Imaging Research Institute (SCIRI) of Nanjing University of Science and Technology, Nanjing, Jiangsu Province 210019, China*
[c] *Jiangsu Key Laboratory of Visual Sensing & Intelligent Perception, Nanjing, Jiangsu Province 210094, China*
[d] *State key Laboratory of Extreme Environment Optoelectronic Dynamic Measurement Technology and Instrument, Taiyuan, Shanxi Province 030051, China*

ARTICLE INFO

Keywords:
Fourier ptychographic diffraction tomography
Three-dimensional microscopy
Dark-field imaging
Non-matched illumination

ABSTRACT

Non-interferometric optical diffraction tomography (ODT) offers a powerful route for three-dimensional (3D), label-free imaging of live biological cells. However, in high-numerical-aperture (NA) systems, its performance is fundamentally limited by the geometry of standard multi-well culture plates, which restrict oblique illumination angles and prevent the matched illumination condition required for accurate tomographic reconstruction. This mismatch causes a physical loss of low-frequency information in the recorded intensity, traditionally regarded as a major barrier to high-resolution ODT. Here, we demonstrate that such non-matched illumination can instead be harnessed as an intrinsic mechanism for dark-field-like contrast enhancement, without additional measurements or post-processing. This insight underpins our proposed method: dark-field Fourier ptychographic diffraction tomography (DF-FPDT). By selectively updating only the high-frequency components inherently encoded in intensity measurements, DF-FPDT naturally suppresses low-frequency background and enhances fine subcellular structures, mimicking the behavior of dark-field microscopy while preserving the non-interferometric, volumetric, and quantitative advantages of FPDT. Validated through simulations and experiments on 3D micro-phantom, microspheres, and COS-7 cells, DF-FPDT demonstrates robust, high-contrast 3D imaging under standard microscope configurations and culture conditions. By leveraging what was once considered a constraint, DF-FPDT offers a compact and practical solution for dynamic 3D live-cell imaging in realistic biological environments.

1. Introduction

The ability to non-invasively cultivate and observe biological cells in situ under standardized culture conditions is fundamental for advancing our understanding of cellular behaviors, dynamics, and responses to microenvironmental cues [1–3]. Modern biological research increasingly relies on imaging techniques that enable continuous monitoring of live cells without introducing exogenous labels or perturbations that may alter their native state [4–6]. Among various label-free imaging modalities, optical diffraction tomography (ODT) has emerged as a powerful tool for three-dimensional (3D) visualization of transparent biological specimens by quantitatively reconstructing their intrinsic refractive index (RI) distribution, which correlates with cellular morphology and composition [7–11].

In particular, non-interferometric ODT provides a simple, stable, and alignment-insensitive approach for RI-based imaging, eliminating the need for complex interferometric setups while still achieving 3D structural reconstruction [12–18]. This makes it highly attractive for

---

Peer review under responsibility of Xi'an Institute of Optics and Precision Mechanics, CAS.

* Corresponding author at: Jiangsu Key Laboratory of Visual Sensing & Intelligent Perception, Nanjing, Jiangsu Province 210094, China.

** Corresponding author at: Smart Computational Imaging Laboratory (SCILab), School of Electronic and Optical Engineering, Nanjing University of Science and Technology, Nanjing, Jiangsu Province 210094, China.

E-mail addresses: chenqian@njust.edu.cn (Q. Chen), zuochao@njust.edu.cn (C. Zuo).

[1] These authors contributed equally to this work.

https://doi.org/10.1016/j.iopt.2025.100006
Received 7 July 2025; Received in revised form 17 July 2025; Accepted 6 August 2025

integration with conventional microscope systems and biological laboratories. However, the practical implementation of non-interferometric ODT faces significant challenges when applied to live-cell imaging within standard cell culture plates, such as multi-well plates, which are indispensable for high-throughput studies and controlled microenvironment cultivation [19,20]. A critical technical bottleneck arises from the geometric constraints imposed by these multi-well culture plates, which inherently limit the range of accessible oblique illumination angles. In high numerical aperture (NA) microscopes, where maximizing resolution and imaging performance is desirable, these restrictions prevent the realization of matched illumination condition, a prerequisite for accurate tomographic reconstruction in conventional non-interferometric ODT schemes [12,14,21,22]. Consequently, the missing illumination angles lead to low-frequency information loss in the reconstructed tomograms, which manifests as blurring of structural details, compromised image contrast, and degraded visualization of fine subcellular features.

To overcome this limitation, our group recently proposed an effective solution to circumvent the matched illumination condition by combining Fourier ptychographic diffraction tomography (FPDT) [13, 23] with transport-of-intensity measurements [24–26], referred to as TI-FPDT [27]. By introducing an additional defocused intensity image at each illumination angle, TI-FPDT enables the accurate reconstruction of both low- and high-frequency components under non-matched illumination condition. However, this approach inevitably relies on mechanical movement to acquire defocused data, leading to increased data volume and acquisition time, which poses challenges for real-time or long-term live-cell imaging. In fact, the intensity data obtained under non-matched illumination inherently contain abundant high-frequency phase information [21]. Without the need for additional measurements or post-processing, this non-matched illumination can instead be harnessed as an advantage, transforming what was once considered a limitation into a mechanism for achieving dark-field-like contrast enhancement and visualizing high-resolution fine structural details [28, 29].

Here, we present an advanced imaging strategy termed dark-field Fourier ptychographic diffraction tomography (DF-FPDT), which strategically leverages the typically detrimental low-frequency information loss under non-matched illumination as a functional advantage. By employing a tailored algorithm that selectively updates only the high-frequency components encoded in intensity measurements, as determined by the system's phase transfer function, DF-FPDT naturally suppresses low-frequency background artifacts while significantly enhancing image contrast and resolution. Importantly, DF-FPDT shares the same data acquisition setup as traditional FPDT, requiring no additional intensity measurements, and can reconstruct the RI distribution with high contrast. This approach enables the recovery of detailed subcellular structures with imaging performance comparable to conventional dark-field microscopy, while preserving the non-interferometric, volumetric, and quantitative intrinsic advantages of FPDT. We validate the effectiveness of DF-FPDT through both numerical simulations, using a 3D micro-phantom to quantitatively assess reconstruction quality, and experimental demonstrations, including imaging of standard microspheres and live biological cells within typical culture environments. By effectively addressing the geometric and optical limitations inherent to conventional non-interferometric ODT, DF-FPDT significantly expands the practical utility of RI-based tomography for non-invasive biological imaging under realistic laboratory conditions. With its capability for high-contrast, high-resolution, label-free 3D imaging, combined with full compatibility with standard microscope platforms and cell culture systems, DF-FPDT represents a highly promising, compact tool for a broad range of applications and provides a practical solution for dynamic 3D live-cell imaging in realistic biological environments.

2. Method

2.1. Principle of dark-field diffraction tomography

In the basic theory of diffraction tomography, the physical quantity of interest to be retrieved is the scattering potential of a thick 3D object, via the following expression:

$$O(\mathbf{x}) = k_0^2\left[n(\mathbf{x})^2 - n_m^2\right] \tag{1}$$

where $k_0 = 2\pi/\lambda$ is the wavenumber, with λ being the illumination wavelength in the free space, while $n(\mathbf{x})$and n_m are the spatial RI distribution of the sample and its surrounding medium, correspondingly. $\mathbf{x} = (\mathbf{x}_T, z) = (x, y, z)$ is a short-hand notation for the 3D spatial coordinate. The well-known Fourier diffraction theorem [30,31] establishes a linear relationship between the first-order scattered field $U_{s1}(\mathbf{x})$ generated by an object under the plane wave illumination $U_{in}(\mathbf{x})$ and the object function $O(\mathbf{x})$. In the Fourier domain, it can be expressed as:

$$\hat{O}(\mathbf{u} - \mathbf{u}_{in}) = 4\pi j u_z \hat{U}_{s1}(\mathbf{u}_T) P(\mathbf{u}_T)\delta\left(u_z - \sqrt{u_m^2 - |\mathbf{u}_T|^2}\right) \tag{2}$$

where $\mathbf{u} = (\mathbf{u}_T, u_z) = (u_x, u_y, u_z)$ represents the 3D spatial frequency coordinates corresponding to $\mathbf{x}$ and $\mathbf{u}_{in} = (\mathbf{u}_{inT}, u_{inz}) = (u_{inx}, u_{iny}, u_{inz})$ is the 3D incident plane wave vector, while j is the imaginary unit and $u_m = n_m/\lambda$ is the spatial frequency in the medium n_m. $\widehat{O}(\mathbf{u})$ and $\widehat{U}_{s1}(\mathbf{u}_T)$correspond to the 3D and 2D Fourier transforms of $O(\mathbf{x})$and $U_{s1}(\mathbf{x}_T)$, respectively. $P(\mathbf{u}_T)\delta\left(u_z - \sqrt{u_m^2 - |\mathbf{u}_T|^2}\right)$ is defined as the 3D coherent transfer function, whose spectrum support domain is a restricted Ewald sphere limited by the objective aperture.

According to the theorem described in Eq. (2), for each illumination angle, only a partial spherical cap bounded by the generalized aperture can be probed. By illuminating the object from different angles, distinct regions of the object's frequency spectrum are shifted into the fixed collection aperture of the microscope objective, thereby expanding the accessible frequency domain of the object. In conventional ODT systems, the complex amplitude of the total field $U(\mathbf{x}_T)$, is measured by interferometric or holographic approaches. Based on these measurements, $U_{s1}(\mathbf{x}_T)$can be further calculated using either first-order Born approximation or Rytov approximation [8,30,32], and then mapped on the particular Ewald sphere according to Eq. (2). Fig. 1a illustrates the illumination schematic, while Fig. 1b shows the corresponding 2D and 3D spectral supports for each illumination angle in a conventional ODT system. It is worth noting that we approximately consider biological cells to be transparent pure phase objects, whose scattering potential spectrum exhibits conjugate symmetry. Therefore, the first-order scattered field obtained from a single measurement can be updated onto two conjugate-symmetric Ewald spherical shells in the scattering potential spectrum, centered at the origin. By collecting a series of angle-dependent interferometric complex field measurements, a substantial portion of the object's 3D Fourier spectrum can be accessed, enabling the reconstruction of the 3D scattering potential of the sample [third column of Figs. 1a and 1b].

For non-interferometric ODT based on intensity-only measurements, we cannot directly measure the complex amplitude of the total field since the inherent intensity recording leads to the loss of the phase component. However, the phase component of the scattered field decisively contains the information about the RI distribution of samples. Therefore, the key to non-interferometric ODT implementation is the encoding of phase information into intensity images through modulations and the recovery of the desired phase component using phase retrieval algorithms during the reconstruction process. Under plane wave illumination, this phase encoding process can be intuitively interpreted from the perspective of the phase transfer function (PTF), which can be expressed as:

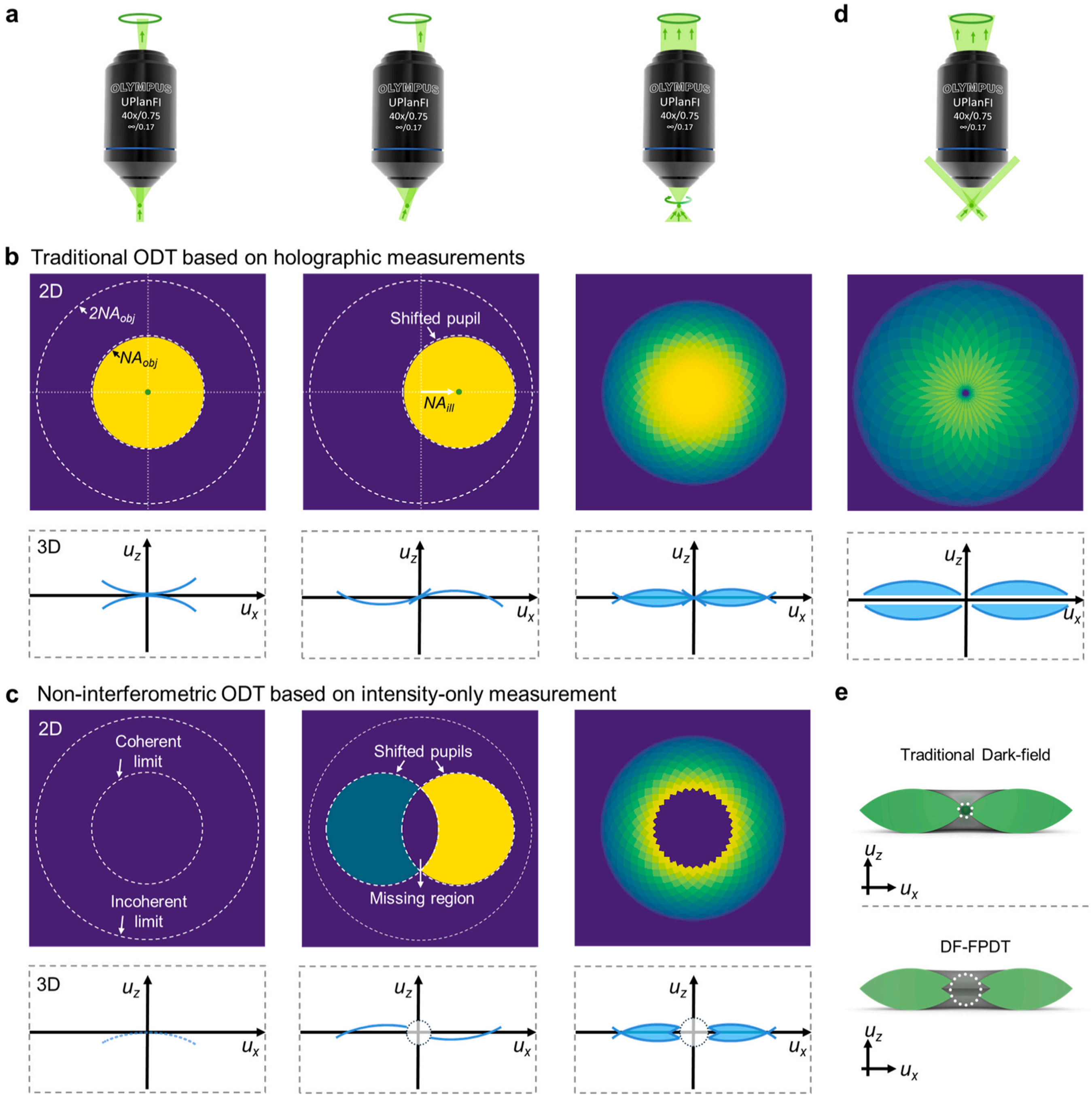

Fig. 1. Principle of holographic diffraction tomography and the dark-field diffraction tomography. a, Schematic diagrams of on-axis illumination, tilted illumination, and angle-scanning illumination. **b**, 2D and 3D spectral supports for traditional ODT implementation based on holographic measurements. **c**, 2D, and 3D spectrum supports for non-interferometric ODT based on intensity-only measurement. **d**, Schematic of dark-field illumination and the corresponding 2D and 3D spectrum supports. **e**, 3D spectral diagram of traditional dark-field imaging and the proposed DF-FPDT approach in u_x-u_z planes.

$$H_P(\mathbf{u}_T) = j[P(\mathbf{u}_T - \mathbf{u}_{inT}) - P(\mathbf{u}_T + \mathbf{u}_{inT})] \tag{3}$$

where $P(\mathbf{u}_T)$ is the 2D circular pupil function with a radius of NA_{obj}/λ. Fig. 1c shows the 2D and 3D spectrum supports for non-interferometric ODT with an aberration free imaging system under different illumination angles. Unlike conventional ODT system, in non-interferometric ODT for a perfectly in-focus imaging system, on-axis illumination ($|\mathbf{u}_{inT}| = 0$) produces no phase contrast because the two anti-symmetrical (positive and negative) pupils cancel each other out, suggesting that the phase structure cannot be observed in this case as shown in the first column Fig. 1c. Increasing the illumination angle makes the two pupils no longer completely overlap, thus rendering phase information visible. However, when the illumination NA cannot match the objective NA, i.e. $0 < |\mathbf{u}_{inT}| < NA_{obj}/\lambda$, low-frequency phase components are always missing in the overlapped region and cannot be transferred into the intensity image, yet, the non-overlap regions represent high-frequency phase components which can still be transferred into the intensity image.

By reframing this disadvantage of non-matched illumination as a functional advantage, dark-field diffraction tomography can be achieved by selectively reconstructing only the high-frequency components inherently encoded in intensity measurements. Under such conditions, the overlapped region of the PTF is zero, and thus, multiplying the corresponding intensity spectrum by the PTF effectively suppresses unwanted low-frequency background artifacts information while preserving only the high-frequency components that are mapped onto the 3D Ewald sphere. As a result, the final updated 3D spectrum resembles that of conventional dark-field imaging, as illustrated in Figs. 1d and 1e. This enables diffraction tomography to reconstruct high-frequency RI distribution under non-matched illumination, mimicking the behavior of dark-field microscopy and yielding comparable image characteristics. Inspired by this principle, we proposed dark-field Fourier ptychographic diffraction tomography based on the traditional FPDT technique under non-matching illumination.

2.2. Hardware implementation of DF-FPDT

The DF-FPDT system is implemented on a commercial inverted bright-field microscope (IX83, Olympus, Japan) equipped with a programmable annular LED array for illumination, as shown in Fig. 2b. The LED array consisted with 28 LED units is controlled by a field-programmable gate array (FPGA, EP4CE10E22C8N, Intel, US), providing narrowband quasi-plane wave illumination (central wavelength: 520 nm, bandwidth: 20 nm). For all experiments, except for polystyrene microspheres imaging, a multi-well cell culture plate (Corning® #3516, polystyrene, sterile) is used. The geometry of the cell culture plate limits the effective illumination NA due to the well height, as illustrated at the bottom of Fig. 2b. The geometry of the cell culture plate imposes a limit on the effective illumination NA, with a maximum value of 0.68 determined by the well height, as shown at the bottom of Fig. 2b. Exceeding this limit would introduce disturbances from the well walls, degrading the quasi-plane wave illumination. To avoid this, the LED array is positioned 32 mm above the sample, providing a maximum illumination NA of 0.65, which is lower than the NA of both dry objectives (UPlanFI 40 ×/0.75 NA and UPLSAPO 40 ×/0.95 NA, Olympus, Japan) and oil-immersion objective (UPLSAPO 100 ×/1.4 NA, Olympus, Japan). Image acquisition is performed using a scientific CMOS camera (ORCA-Flash 4.0, C13440, Hamamatsu, Japan) with 2048 × 2048 resolution and 6.5 μm pixel size. The LED array and camera are

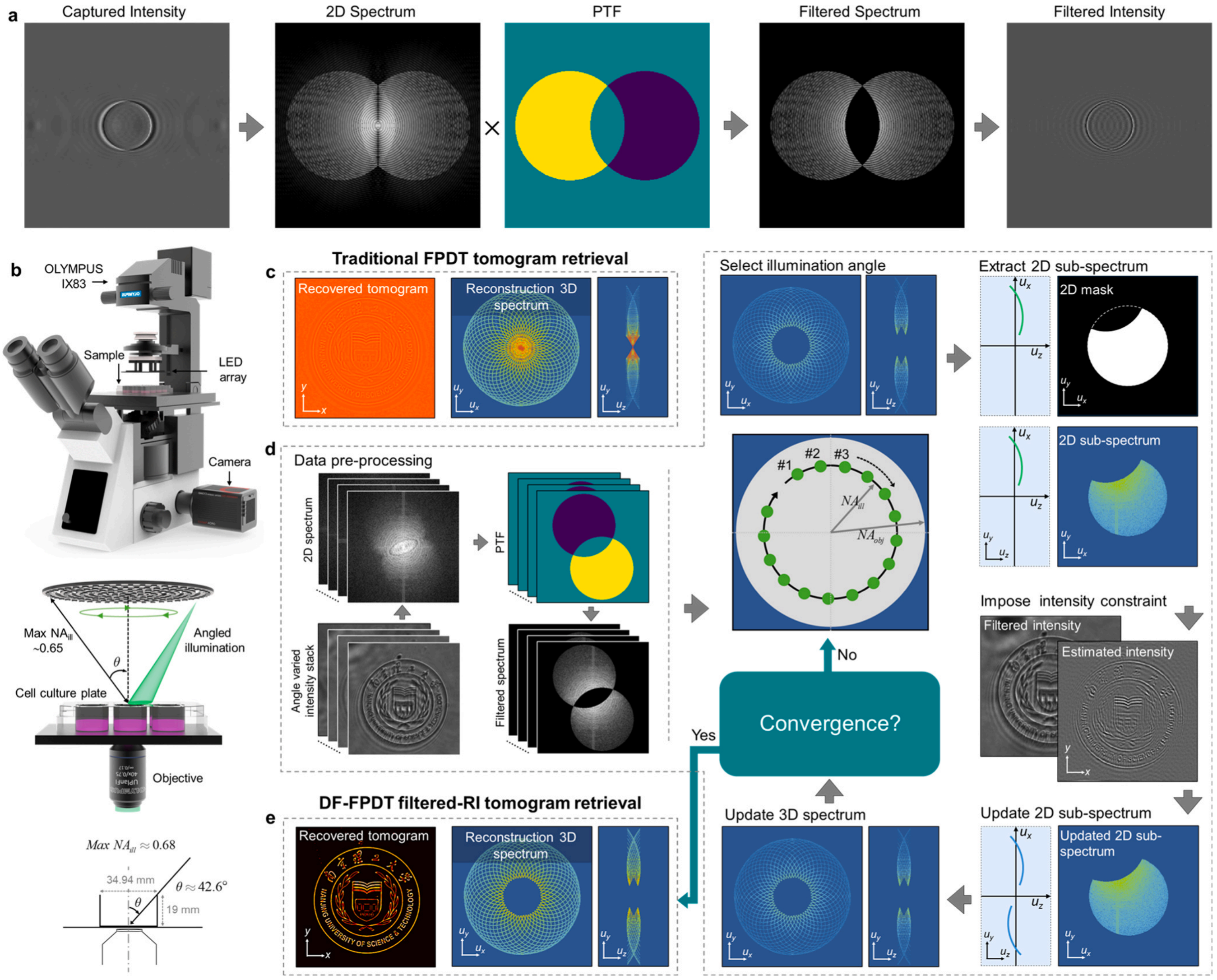

Fig. 2. Hardware implementation and working flow of DF-FPDT. a, Process of intensity filtering via PTF to show how DF-FPDT technique selectively enhances high-frequency components and suppresses low-frequency components. **b**, Schematic of the DF-FPDT system based on a commercial microscope integrated with a programmable angular LED array for illumination. The diagram illustrates the DF-FPDT platform and the geometric constraints imposed by the standard cell culture plate, which limit the maximum accessible illumination NA to match the objective NA. **c**, Representative RI tomogram reconstructed using the conventional FPDT method, highlighting the limitations caused by low-frequency information loss. **d**, Workflow of the DF-FPDT reconstruction algorithm, where only the high-frequency components within the 3D spectrum are selectively updated to enhance image contrast and resolution. **e**, Example of DF-FPDT reconstruction results using the NJUST logo, including both the reconstructed tomogram and the corresponding 3D spectrum, demonstrating the effectiveness of the proposed method in enhancing structural details.

synchronized via the same FPGA controller using two coaxial cables for triggering and exposure monitoring. As each LED unit is sequentially illuminated, 28 full-frame 16-bit angle-varied intensity images are captured. All the experimental data are processed by MATLAB software (MATLAB R2018a) on a computer workstation.

2.3. DF-FPDT reconstruction algorithm

Although the traditional FPDT technique reconstructs the 3D RI distribution of a sample using an angle-varied intensity stack, it consistently suffers from significant low-frequency information loss under non-matched illumination condition. For instance, Fig. 2c shows the 3D spectrum and the reconstructed RI tomogram of the standard logo of Nanjing University of Science and Technology (NJUST), obtained using traditional FPDT under non-matched illumination. While high-frequency components of the RI distribution can be recovered, the substantial loss of low-frequency information and the presence of reconstructed artifacts result in a tomogram with poor contrast, making it challenging to resolve essential structural features. Fig. 2d shows the workflow of the proposed DF-FPDT algorithm for reconstructing the high-frequency components of the 3D RI distribution. The DF-FPDT algorithm provides an iterative solution to the inverse scattering problem by incorporating a filtered intensity constraint within the traditional FPDT reconstruction framework. The DF-FPDT reconstruction process alternates between the spatial domain and the Fourier domain, following the steps outlined below:

Step 1: Perform a Fourier transform on each recorded intensity image to obtain the corresponding 2D intensity spectrum. The intensity spectrum is then multiplied by the corresponding PTF to generate the filtered intensity spectrum. An inverse Fourier transform is subsequently performed to obtain the filtered intensity image in the spatial domain. This process is expressed as:

$$I_F^i(\mathbf{x}_T) = \mathscr{F}^{-1}\{\mathscr{F}\{I^i(\mathbf{x}_T)\} \times H_P^i(\mathbf{u}_T)\} \tag{4}$$

where superscript i represent i^{th} illumination angle.

Step 2: Select a specific illumination angle and project its corresponding Ewald spectrum onto a 2D sub-spectrum. Note that the spectral support domain is no longer a circular Ewald spherical shell, but rather a crescent-shaped support mask determined by the positive region of the phase transfer function (PTF). The inverse Fourier transform is then performed on the 2D sub-spectrum to obtain the first-order scattered field $U_{s1}^i(\mathbf{x}_T)$.

Step 3: Enforce intensity constraint on $U_{s1}^i(\mathbf{x}_T)$ using filtered intensity $I_F^i(\mathbf{x}_T)$ to obtain the updated first-order scattered field $\overline{U}_{s1}^i(\mathbf{x}_T)$. The update formula is

$$\overline{U}_{s1}^i(\mathbf{x}_T) = \ln\left\{\sqrt{I_F^i(\mathbf{x}_T)}\ \frac{\exp\left(U_{s1}^i(\mathbf{x}_T)\right)}{\left|\exp\left(U_{s1}^i(\mathbf{x}_T)\right)\right|}\right\} \tag{5}$$

Step 4: Map the updated 2D sub-spectrum $\overline{U}_{s1}^i(\mathbf{x}_T)$ to the 3D scattering potential spectrum according to Eq. (2). As mentioned before, we approximately consider samples to be transparent pure phase objects and their spectrum to be conjugate symmetry. Therefore, the sub-spectrum is updated to two conjugated symmetric Ewald spherical shells centered at the origin.

Step 5: Select the next illumination angle and repeat Steps 2–4. This process is performed for all illumination angles, completing one full iteration. The entire iterative procedure is repeated for M cycles until the DF-FPDT reconstruction converges with all intensity measurements.

Step 6: Perform a 3D inverse Fourier transform on the converged scattering potential spectrum to obtain the final reconstructed result with high contrast and high resolution, as shown in Fig. 2e.

3. Results

3.1. Validation of DF-FPDT on simulations

To evaluate the effectiveness of DF-FPDT, we conducted numerical simulations using 40 ×/0.95 NA and 100 ×/1.4NA objectives and compared the results with those obtained from the traditional FPDT technique at different axial planes. As discussed earlier, the geometry of the culture plate constrains the illumination NA, making it impossible to match the NA of high-magnification objectives. Therefore, in our simulations, the illumination NA was fixed at 0.65 based on the measured parameters of the culture plate shown in Fig. 2b. Fig. 3a presents the 3D visualization of the ground truth micro-phantom, while Fig. 3b shows the corresponding 2D slices at different axial positions. The first rows of Figs. 3c and 3d display the reconstructed 3D RI distributions using the conventional FPDT technique with 40 ×/0.95 NA and 100 ×/1.4 NA objectives, respectively. Due to the illumination NA being smaller than the objective NAs, the conventional FPDT fails to fully recover the RI distribution of the micro-phantom. In both cases, only the high-frequency details, such as sharp edges, are accurately reconstructed, while the broader low-frequency information is lost. This is because, under non-matched illumination condition, intensity measurements lack the complete complex field information required for accurate 3D RI reconstruction, leading to systematic low-frequency loss and RI underestimation.

Rather than viewing this limitation as a drawback, our proposed DF-FPDT technique strategically exploits it to enhance high-frequency structural reconstruction. As shown by the corresponding 3D spectra, the DF-FPDT selectively updates only the high-frequency components inherently encoded in intensity measurements while suppressing the low-frequency background content. In this way, DF-FPDT transforms the conventional limitation of low-frequency loss into a functional advantage, effectively isolating and enhancing high-frequency structural details. It is important to note that the RI tomograms reconstructed by DF-FPDT no longer represent absolute RI values but correspond to filtered-RI distributions due to the suppression of low spatial frequencies. This filtering enhances contrast in the reconstructed 3D tomograms, as demonstrated in the second rows of Figs. 3c and 3d, and theoretically resembles the contrast-enhancement mechanism of conventional dark-field microscopy.

Furthermore, comparing the results obtained with the 40 ×/0.95 NA and 100 ×/1.4 NA objectives highlights the superior optical sectioning capability of the higher NA objective. For example, the 40 ×/0.95 NA tomograms in Fig. 3c exhibit significant contributions from neighboring axial planes at each axial position, whereas the 100 ×/1.4 NA results in Fig. 3d provide stronger optical sectioning, effectively isolating structures at each axial plane with minimal interference from adjacent planes. These results demonstrate that our method overcomes the constraint of matched illumination condition, enabling the use of higher NA objective lenses to improve lateral and axial resolution without the need to modify the illumination configuration.

3.2. Simulations and experimental verification using polystyrene microspheres

To further validate the proposed DF-FPDT method, both simulations and experimental measurements were performed using a pure phase microsphere as the test sample, with optical parameters matching those of the polystyrene microspheres and the imaging system used in the experiments. An ideal microsphere with a diameter of 15 μm and a RI of 1.60 was immersed in a surrounding medium with RI of 1.58. Sequential angle-varied plane wave illumination was applied with a fixed illumination NA of 0.65 and a central wavelength of 520 nm, resulting in 28 intensity images captured under both matched (40 ×/0.65 NA objective) and non-matched (40 ×/0.95 NA and 100 ×/1.4 NA objectives) illumination conditions. Cross-sectional slices of the reconstructed 3D RI

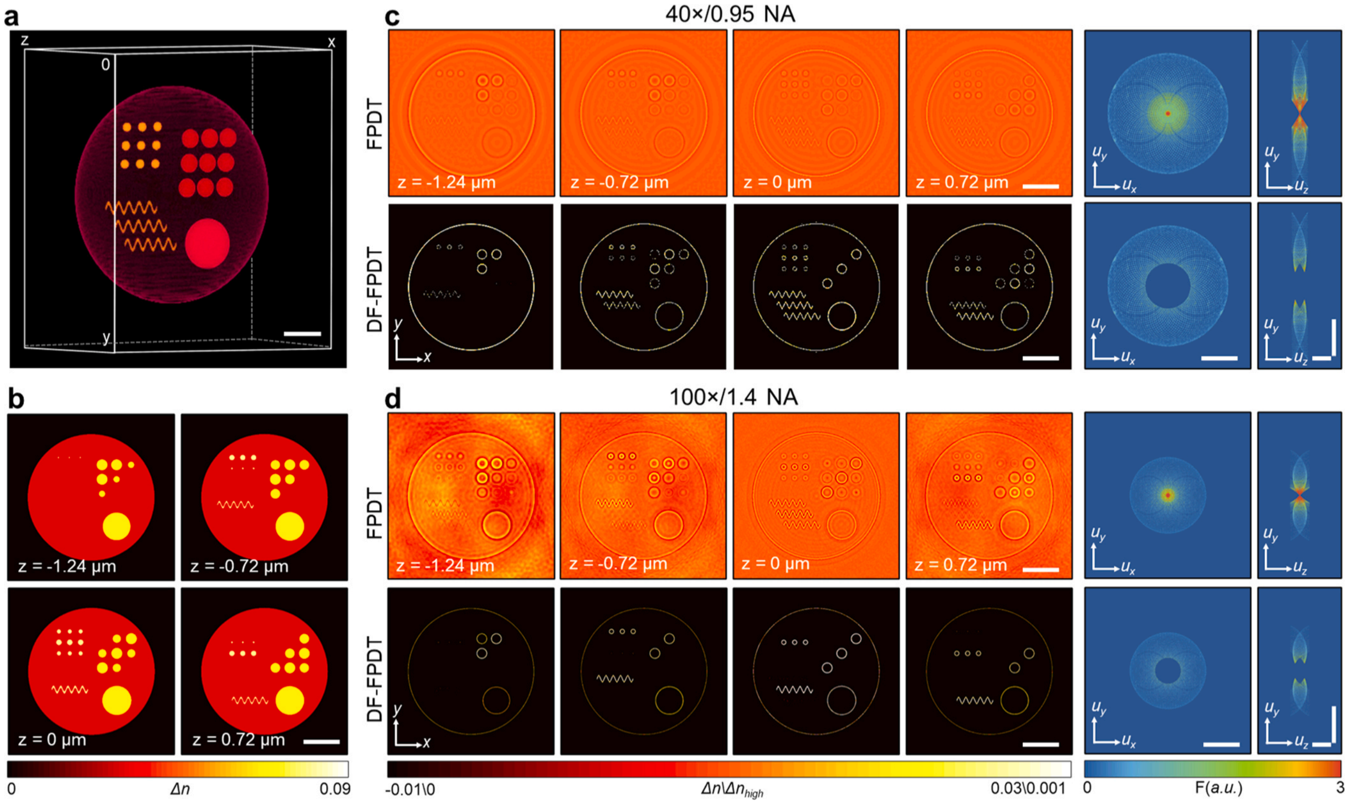

Fig. 3. Simulation comparison of 3D tomographic imaging using FPDT and DF-FPDT with 40 ×/0.95 and 100 ×/1.4 NA objectives. **a**, **b**, 3D rendering, and 2D slice views of the ground truth micro-phantom. **c**, **d**, Reconstructed tomograms at different axial planes using 40 ×/0.95 and 100 ×/1.4 NA objectives, respectively, along with their 3D spectra. Scale bars: (**a**) 5 μm, (**b**–**e**) 10 μm.

distributions in the x–y and y–z planes are shown in Fig. 4. Figs. 4a and 4d present the simulated and experimental RI slices reconstructed using the conventional FPDT technique under matched illumination condition ($NA_{ill} = NA_{obj} = 0.65$). In this case, both low- and high-frequency components are successfully recovered. On the other hand, under non-matched illumination condition ($NA_{ill} < NA_{obj}$), the reconstructed RI distributions exhibit pronounced low-frequency information loss in both simulation and experimental results, as shown in the first columns of Figs. 4b, 4c, 4e, and 4f. Only high-frequency structural details, such as sharp edges, are accurately reconstructed. The second column of Figs. 4b, 4c, 4e, and 4f show the RI distributions obtained using the DF-FPDT method, in which low-frequency background components are intentionally removed. By leveraging the non-matched illumination condition, DF-FPDT enhances image contrast and emphasizes the microspheres boundaries, consistent with theoretical expectations. Additionally, quantitative evaluations are performed for microsphere imaging. The Structural Similarity Index (SSIM) values between the simulated (ground truth) and experimental DF-FPDT results are above 0.9 for both the dry 40 ×/0.95 NA objective and the oil immersion 100 ×/1.4 NA objective, indicating strong structural similarity and validating the DF-FPDT approach. Furthermore, Edge of Gradient (EOG) values for DF-FPDT are significantly higher than those for traditional FPDT, demonstrating enhanced contrast in the reconstructed images, consistent with the observed structural improvements. Furthermore, both the simulation and experimental results demonstrate good agreement under matched and non-matched illumination conditions, confirming the validity and effectiveness of the DF-FPDT approach.

3.3. *Dynamic imaging of live COS-7 cells*

To demonstrate the applicability of the DF-FPDT technique to biological cells, we performed dynamic imaging of live COS-7 cells. The high-resolution, high-contrast imaging capability of DF-FPDT provides a distinct advantage for label-free time-lapse imaging of COS-7 cells within multi-well cell culture plates. As previously mentioned, due to the constraints of the cell culture plate, the illumination NA was fixed at 0.65 for all experiments, and COS-7 cells were imaged using both a dry 40 ×/0.95 NA objective and an oil-immersion 100 ×/1.4 NA objective lens. To validate the DF-FPDT results, COS-7 cells were labeled with MitoTracker to specifically mark mitochondria, followed by fluorescence (FL) imaging to confirm their locations. The FL images were then merged with the DF-FPDT reconstructions, demonstrating the effectiveness and biological relevance of the DF-FPDT technique.

Fig. 5a shows the tomograms reconstructed by FPDT and DF-FPDT, FL image, and merged image of live COS-7 cells at z = 0 μm at the initial time point, acquired using a 40 ×/0.95 NA objective. Due to the mismatch between the illumination NA and objective NA in this configuration (illumination NA is significantly lower than the objective NA), the conventional FPDT technique fails to accurately reconstruct the low-frequency RI components of COS-7 cells. While organelles with inherently high RI values, such as lipid droplets, are visible, the contrast of other subcellular structures, including mitochondria, remains insufficient. Their RI values are close to those of the background, hindering clear visualization in the reconstructed tomogram. After applying DF-FPDT to filter out low-frequency components and enhance small-scale structural contrast, the reconstructed tomogram reveals subcellular organelles, including mitochondria, with significantly improved resolution and contrast. The third image in Fig. 5a displays the corresponding FL image, while the fourth image presents the merged result of the RI tomogram and FL image. The merged image confirms that the worm-like, bent, and twisted structures in the RI tomogram correspond to mitochondria, as they perfectly overlap with mitochondria-specific fluorescence labeled by MitoTracker. To further demonstrate the dynamic visualization capability of DF-FPDT, Figs. 5b and 5c present time-

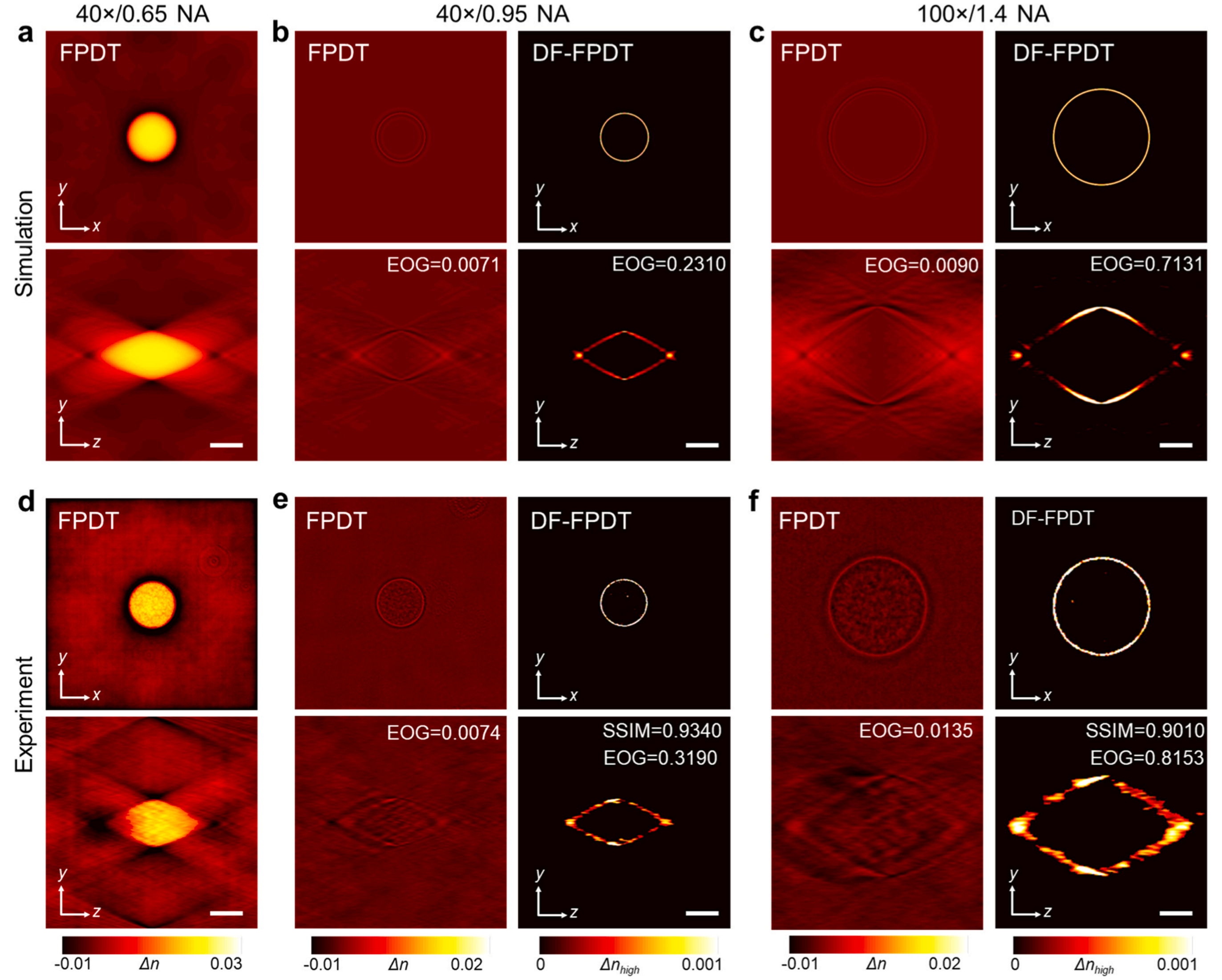

Fig. 4. Simulation and experimental results of 15 µm diameter polystyrene microspheres with different objectives. a–c, Simulated lateral and axial reconstructed slices of microspheres using FPDT and DF-FPDT with different objectives. **d–f**, Experimental lateral and axial reconstructed slices of microsphere using FPDT and DF-FPDT with different objective lenses. Scale bars: (**a**,**b**,**d**,**e**)10 µm, (**c**,**f**) 5 µm.

lapse imaging results of two enlarged regions of interest (ROIs) selected from Fig. 5a. In ROI1 [Fig. 5b], the yellow and white arrows highlight the fusion process of two individual mitochondria over time, ultimately forming a larger mitochondrial structure. In ROI2 [Fig. 5c], blue arrows indicate the movement of a lipid droplet across different time points. As the lipid droplet interacts with nearby mitochondria, it induces visible changes in mitochondrial morphology, illustrating the dynamic interplay between lipid droplets and mitochondria. These dynamic processes are further validated by the corresponding FL images (third row) and the merged images (fourth row) in Figs. 5b and 5c, where the fluorescence-labeled structures exhibit perfect spatial overlap with the DF-FPDT results at each time point. Additionally, a comparison of time-lapse imaging results between FPDT and DF-FPDT, along with the time-lapse merged images with FL data, is provided in Visualization 1. Furthermore, EOG values for DF-FPDT are significantly higher than those for traditional FPDT, confirming the enhanced contrast and sharper structural details in the reconstructed images.

Fig. 6 further demonstrates dynamic RI imaging of another live COS-7 cell across different time points, acquired using a 100 × oil-immersion objective. Fig. 6a displays the reconstructed RI tomogram, FL image, and the merged image. The merged image confirms that the mitochondrial structures in the FL image perfectly overlap with the high-contrast features revealed by the RI reconstruction. To better visualize subcellular dynamics over time, magnified ROIs are shown in Figs. 6b and 6c. In ROI1, two distinct mitochondria are clearly visible at the 0:30-min time point (indicated by white arrows). These mitochondria subsequently fuse to form a larger structure by 2:00 min, followed by fission at 3:20 min, resulting in two separate mitochondrial structures. In ROI2, the white dashed rectangle highlights a small, rod-like mitochondrion at the beginning of the observation, which transforms into a circular structure by 3:20 min. The blue dashed rectangle further illustrates mitochondrial fission events at three different time points. These dynamic processes, including mitochondrial fusion, fission, and morphological changes, are further validated by the corresponding FL images (third row) and merged results (fourth row) in Figs. 6b and 6c, where the FL signals exhibit excellent spatial agreement with the RI reconstructions at each time point. To further illustrate the dynamic processes, the time-lapse visualization showing DF-FPDT results, FL images, and merged reconstructions is provided in Visualization 2. Additionally, EOG values for DF-FPDT are significantly higher than those for traditional FPDT, demonstrating the superior contrast achieved by DF-FPDT in the dynamic imaging of live COS-7 cells.

These experimental results highlight the capability of DF-FPDT to achieve high-resolution, high-contrast, label-free imaging of live cells

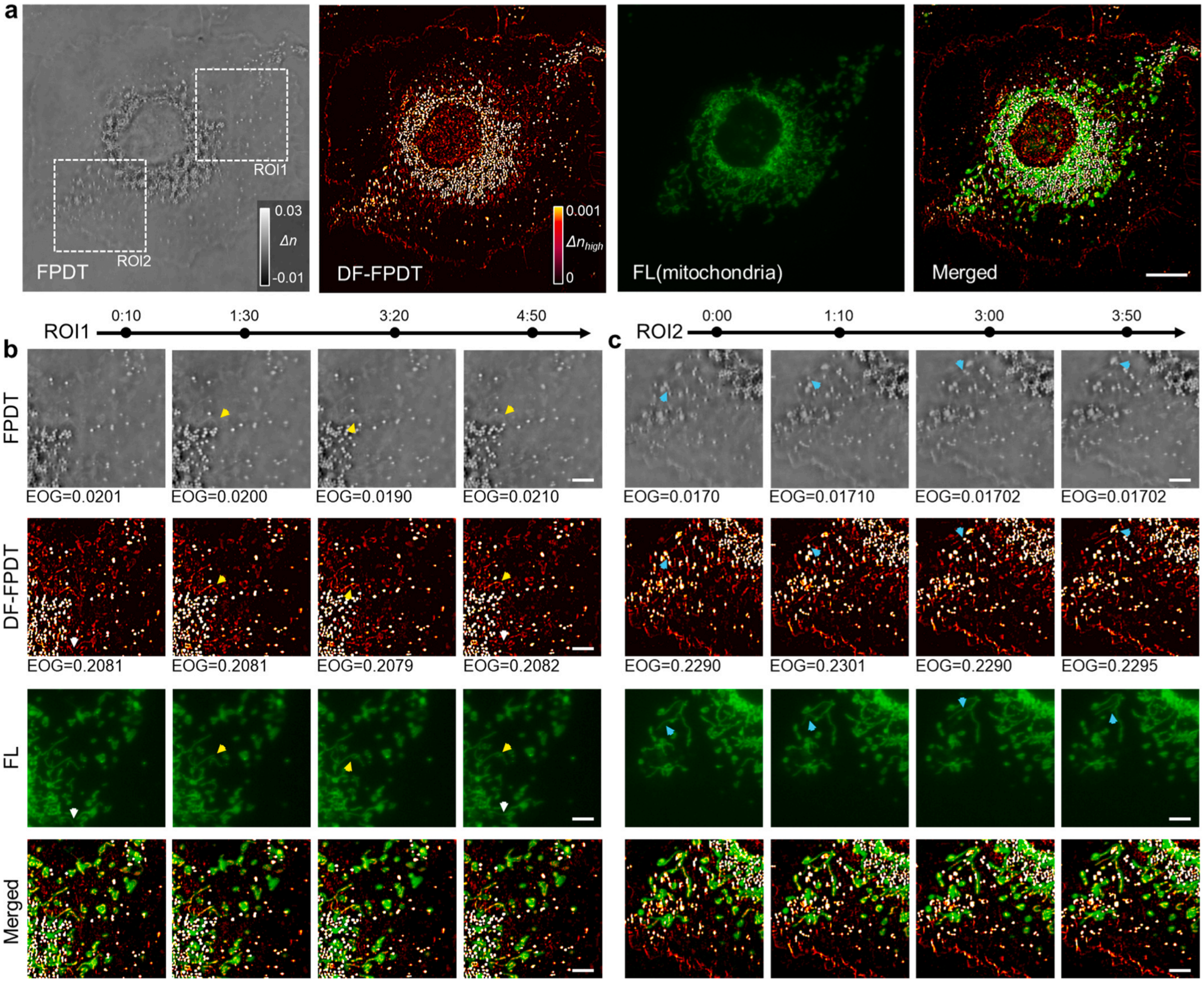

Fig. 5. Time-lapse high-resolution imaging of live COS-7 cells supplemented with wide-field fluorescence imaging of mitochondria, using a 40 ×/0.95NA objective. **a**, Tomograms reconstructed by FPDT and DF-FPDT at the focal plane, the corresponding fluorescence image, and the merged image of DF-FPDT and fluorescence at the initial time point. **b**,**c**, Time-lapse reconstructed slices with FPDT and DF-FPDT, fluorescence images, and merged results for the ROIs in (**a**). Scale bars: (**a**) 15 μm, (**b**,**c**) 5 μm.

under non-matched illumination condition, making it well-suited for cell cultivation and observation within standard cell culture plate environments. More importantly, this method overcomes the constraints of matched illumination condition, enabling the use of higher NA objective lenses to improve both lateral and axial resolution without the need to modify the illumination configuration.

4. Conclusion

In this study, we have presented DF-FPDT, a novel imaging strategy designed to overcome the limitations imposed by standard multi-well culture plates in high-NA optical systems. Traditionally, non-matched illumination condition in non-interferometric ODT result in the loss of low-frequency information due to restricted oblique illumination angles caused by the geometry of standard multi-well cell culture plates, which has been a significant barrier to achieving high-contrast and high-resolution imaging. However, we demonstrate that this non-matched illumination can be harnessed as an advantage, transforming what was once considered as a limitation into a mechanism for achieving dark-field-like contrast and improving the resolution of subcellular structures. DF-FPDT uniquely addresses the issue by selectively updating the high-frequency components during the reconstruction process, thus suppressing the low-frequency background and enhancing fine structural details. This approach mimics the behavior of contrast enhancement of dark-field microscopy while maintaining the volumetric, quantitative, and non-interferometric advantages of FPDT. Extensive numerical simulations and experimental validations on 3D micro-phantom, microspheres, and live cells confirm the capability of DF-FPDT to deliver high-contrast, high-resolution, label-free 3D imaging, while remaining fully compatible with standard microscope setups and widely used cell culture plates. By eliminating the need for complex optical setups or additional defocused measurements in traditional interferometric or non-interferometric ODT, DF-FPDT offers a simple, stable, and practical solution for non-invasive live-cell imaging and dynamic cellular monitoring. Overall, DF-FPDT represents a powerful, compact solution for overcoming the challenges of live-cell imaging, significantly expanding the applicability of RI-based tomography under realistic laboratory conditions. Its simplicity, high-resolution capabilities, and compatibility with standard laboratory setups make it a promising tool for advancing a wide range of biological and biomedical applications, including live-cell imaging, high-throughput drug screening, and cellular analysis.

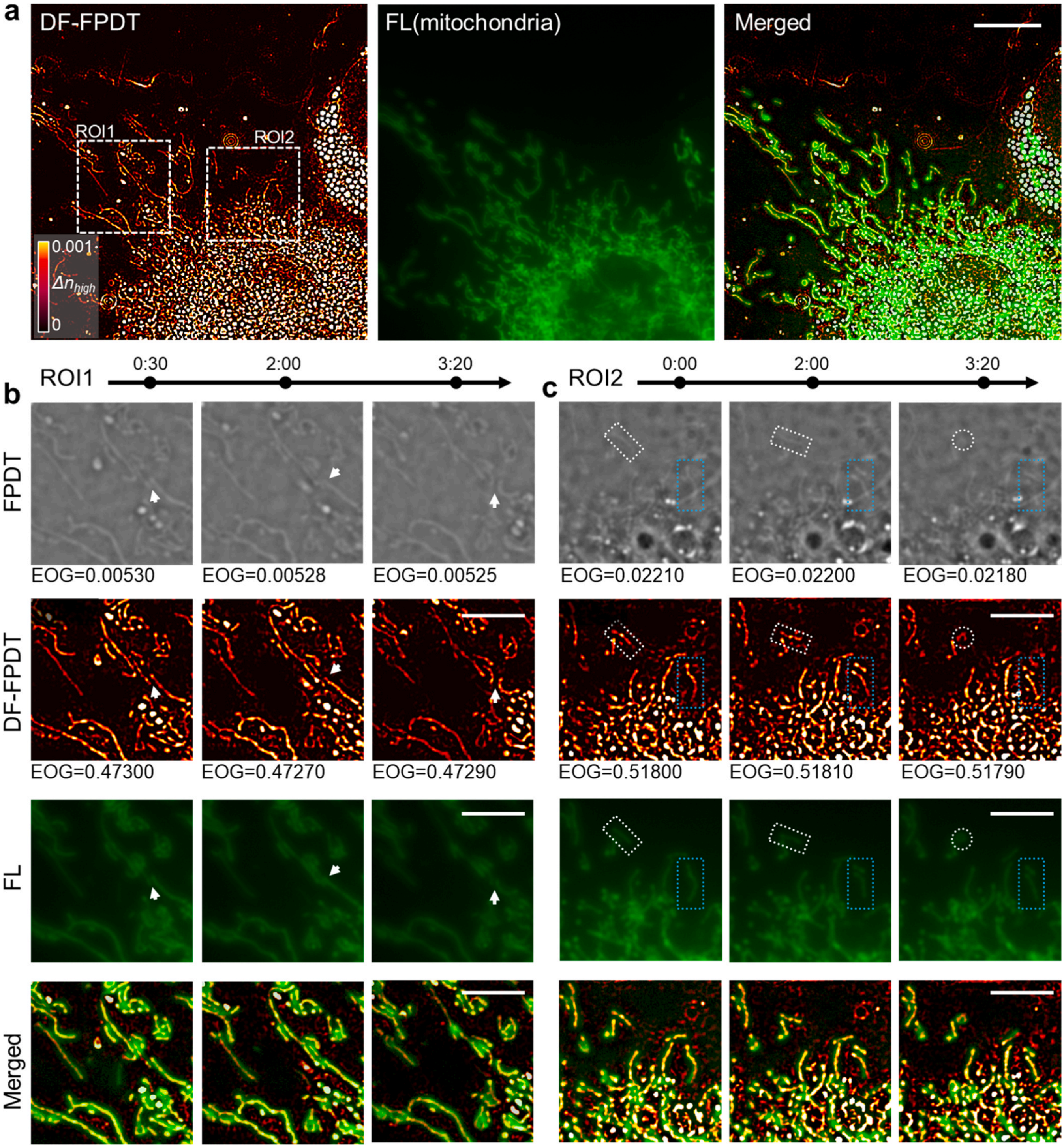

Fig. 6. Time-lapse high-resolution imaging of live COS-7 cells supplemented with wide-field fluorescence imaging of mitochondria, using a 100 ×/1.4NA objective. **a**, Reconstructed tomogram using DF-FPDT, the corresponding fluorescence image, and the merged image at the focal plane at the initial time point. **b**, **c**, Time-lapse reconstructed slices of FPDT and DF-FPDT, fluorescence images, and merged results for the ROIs in (**a**). Scale bars: (**a**)10 μm, (**b**,**c**) 5 μm.

Despite its advantages, DF-FPDT also presents some limitations. Because the method is specifically designed to suppress low-frequency components, it reconstructs a filtered RI distribution rather than absolute RI values. This makes it particularly effective for enhancing contrast in high-frequency structural features, but less suitable for applications that require precise absolute RI quantification. For such tasks, methods like our previously reported TI-FPDT, which recovers full-spectrum RI using defocused measurements, are more appropriate. In the future, DF-FPDT could serve as part of a dual-mode imaging strategy, allowing users to alternate between contrast-optimized and full-RI reconstruction modes depending on the imaging task. Additionally, data-driven approaches such as deep learning-based reconstruction or prior-informed inversion may offer a path toward estimating low-frequency content without additional acquisitions, potentially expanding the applicability of DF-FPDT to broader quantitative imaging tasks. Further improvements could also be achieved by optimizing the LED array design or integrating adaptive illumination strategies to enhance speed and contrast in real-time imaging scenarios.

Author contributions

H. Ullah and S. Zhou contributed equally to this work.

C. Zuo, H. Ullah, and S. Zhou developed the theoretical description of the method.

H. Ullah, K. Du, and Z. Bai performed the experiments and simulations.

H. Ullah and S. Zhou performed the data analysis.

All authors participated in discussions during the development of the paper.

C. Zuo and Q. Chen conceived and supervised this project.

All authors contributed to writing and correcting the manuscript.

Funding

This work was supported by the National Natural Science Foundation of China (62227818, 62361136588, 62305162, U21B2033), National Key Research and Development Program of China (2022YFA1205002, 2024YFE0101300, 2024YFF0505603, 2024YFF0505600), Biomedical Competition Foundation of Jiangsu Province (BE2022847), Key National Industrial Technology Cooperation Foundation of Jiangsu Province (BZ2022039), Fundamental Research Funds for the Central Universities (30923010206, 2023102001, 2024202002), National Key Laboratory of Plasma Physics (JCKYS2024212804), and Open Research Fund of Jiangsu Key Laboratory of Spectral Imaging & Intelligent Sense (JSGP202105, JSGP202201, JSGPCXZNGZ202401).

Competing interests

The authors declare no conflicts of interest.

Acknowledgments

We thank Dr. Ran Ye for preparing NJUST logo sample.

Data Availability

Data underlying the results presented in this paper are not publicly available at this time but may be obtained from the authors upon reasonable request.

References

[1] W.H. Abuwatfa, W.G. Pitt, G.A. Husseini, Scaffold-based 3D cell culture models in cancer research, J. Biomed. Sci. 31 (2024) 7.
[2] S.G. Klein, S.M. Alsolami, S. Arossa, G. Ramos-Mandujano, A.J. Parry, A. Steckbauer, et al., In situ monitoring reveals cellular environmental instabilities in human pluripotent stem cell culture, Commun. Biol. 5 (2022) 119.
[3] H. Ryoo, H. Kimmel, E. Rondo, G.H. Underhill, Advances in high throughput cell culture technologies for therapeutic screening and biological discovery applications, Bioeng. Transl. Med. 9 (2024) e10627.
[4] P. Gao, B. Yao, I. Harder, N. Lindlein, F.J. Torcal-Milla, Phase-shifting zernike phase contrast microscopy for quantitative phase measurement, Opt. Lett. 36 (2011) 4305.
[5] Y. Park, C. Depeursinge, G. Popescu, Quantitative phase imaging in biomedicine, Nat. Photonics 12 (2018) 578–589.
[6] C.E. Serafini, S. Charles, P. Casteleiro Costa, W. Niu, B. Cheng, Z. Wen, et al., Non-invasive label-free imaging analysis pipeline for in situ characterization of 3D brain organoids, Sci. Rep. 14 (2024) 22331.
[7] D. Jin, R. Zhou, Z. Yaqoob, P.T.C. So, Tomographic phase microscopy: principles and applications in bioimaging [invited], J. Opt. Soc. Am. B 34 (2017) B64.
[8] Y. Sung, W. Choi, C. Fang-Yen, K. Badizadegan, R.R. Dasari, M.S. Feld, Optical diffraction tomography for high resolution live cell imaging, Opt. Express 17 (2009) 266–277.
[9] Y. Cotte, F. Toy, P. Jourdain, N. Pavillon, D. Boss, P. Magistretti, et al., Marker-free phase nanoscopy, Nat. Photonics 7 (2013) 113–117.
[10] K. Kim, J. Yoon, S. Shin, S. Lee, S.-A. Yang, Y. Park, Optical diffraction tomography techniques for the study of cell pathophysiology, J. Biomed. Photonics Eng. (2016) 020201–1-020201–16.
[11] A. Kuś, M. Dudek, B. Kemper, M. Kujawińska, A. Vollmer, Tomographic phase microscopy of living three-dimensional cell cultures, J. Biomed. Opt. 19 (2014) 1.
[12] J. Li, N. Zhou, J. Sun, S. Zhou, Z. Bai, L. Lu, et al., Transport of intensity diffraction tomography with non-interferometric synthetic aperture for three-dimensional label-free microscopy, Light Sci. Appl. 11 (2022) 154.
[13] C. Zuo, J. Sun, J. Li, A. Asundi, Q. Chen, Wide-field high-resolution 3D microscopy with Fourier ptychographic diffraction tomography, Opt. Lasers Eng. 128 (2020) 106003.
[14] Y. Baek, Y. Park, Intensity-based holographic imaging via space-domain Kramers–Kronig relations, Nat. Photonics 15 (2021) 354–360.
[15] J. Li, A.C. Matlock, Y. Li, Q. Chen, C. Zuo, L. Tian, High-speed in vitro intensity diffraction tomography, Adv. Photonics 1 (2019) 1.
[16] S. Chowdhury, M. Chen, R. Eckert, D. Ren, F. Wu, N. Repina, et al., High-resolution 3D refractive index microscopy of multiple-scattering samples from intensity images, Optica 6 (2019) 1211.
[17] J.M. Soto, J.A. Rodrigo, T. Alieva, Label-free quantitative 3D tomographic imaging for partially coherent light microscopy, Opt. Express 25 (2017) 15699.
[18] M. Chen, L. Tian, L. Waller, 3D differential phase contrast microscopy, Biomed. Opt. Express 7 (2016) 3940–3950.
[19] M.A. Freyberg, P. Friedl, The use of a conventional tissue culture plate as an optically accessible perfusion chamber for in situ assays and for long-term cultivation of mammalian cells, Cytotechnology 26 (1998) 49–58.
[20] V.K.R. Lekkala, S.-Y. Kang, J. Liu, S. Shrestha, P. Acharya, P. Joshi, et al., A pillar/perfusion plate enhances cell growth, reproducibility, throughput, and user friendliness in dynamic 3D cell culture, ACS Biomater. Sci. Eng. 10 (2024) 3478–3488.
[21] J. Sun, C. Zuo, J. Zhang, Y. Fan, Q. Chen, High-speed Fourier ptychographic microscopy based on programmable annular illuminations, Sci. Rep. 8 (2018) 7669.
[22] J. Wang, X. Zhao, Y. Wang, D. Li, Transport-of-intensity differential phase contrast imaging: defying weak object approximation and matched-illumination condition, Photonics Res. 12 (2024) 2712.
[23] S. Zhou, J. Li, J. Sun, N. Zhou, Q. Chen, C. Zuo, Accelerated Fourier ptychographic diffraction tomography with sparse annular LED illuminations, J. Biophotonics 15 (2022).
[24] C. Zuo, J. Li, J. Sun, Y. Fan, J. Zhang, L. Lu, et al., Transport of intensity equation: a tutorial, Opt. Lasers Eng. 135 (2020) 106187.
[25] C. Zuo, Q. Chen, W. Qu, A. Asundi, Noninterferometric single-shot quantitative phase microscopy, Opt. Lett. 38 (2013) 3538.
[26] L. Waller, L. Tian, G. Barbastathis, Transport of intensity phase-amplitude imaging with higher order intensity derivatives, Opt. Express 18 (2010) 12552–12561.
[27] S. Zhou, J. Li, J. Sun, N. Zhou, H. Ullah, Z. Bai, et al., Transport-of-intensity Fourier ptychographic diffraction tomography: defying the matched illumination condition, Optica 9 (2022) 1362–1373.
[28] T. Chang, S. Shin, M. Lee, Y. Park, Computational approach to dark-field optical diffraction tomography, APL Photonics 5 (2020) 040804.
[29] Z. Meng, L. Ding, S. Feng, F. Xing, S. Nie, J. Ma, et al., Numerical dark-field imaging using deep-learning, Opt. Express 28 (2020) 34266.
[30] E. Wolf, Three-dimensional structure determination of semi-transparent objects from holographic data, Opt. Commun. 1 (1969) 153–156.
[31] V. Lauer, New approach to optical diffraction tomography yielding a vector equation of diffraction tomography and a novel tomographic microscope, J. Microsc. 205 (2002) 165–176.
[32] A.J. Devaney, Inverse-scattering theory within the Rytov approximation, Opt. Lett. 6 (1981) 374.